MEMS Resonant Mass Sensor With Integrated Optical Manipulation

Ethan G. Keeler [ID], Peifeng Jing, Jingda Wu [ID], Chen Zou [ID], and Lih Y. Lin [ID]

Abstract—**We investigate optical manipulation of particles in fluid as a viable method to achieve better experimental fidelity and extend the application of integrated-fluidic resonant-mass sensing. Fluctuations in sample position or trajectory can lead to measurement error, thereby degrading the resolution with which these devices can accurately characterize mass. Optical trapping offers precise location control in such fluidic environments and can define and fix position to mitigate variability, but requires a novel approach to design, fabrication, and biological viability concerns. Optical considerations are especially imperative when working with biological cells, organic matter, or other materials adversely affected by imposing high intensity laser light, and mandate the use of a photonic-crystal structure. Given these requirements, this letter details a design and fabrication approach embodied by unique devices that demonstrate compatibility with optical trapping and mass sensing. Accordingly, the effects of optical manipulation on the measurement are disclosed, toward long-term biological mass monitoring and sensing. Ultimately, precise measurement of singular cell mass could answer many fundamental biological questions, with implications in cell biology, pharmacology, and medicine.**

Index Terms—**MEMS resonators, microfluidics, mass sensing, optical trapping, optical tweezers.**

I. INTRODUCTION

MEMS and NEMS resonant mass sensing devices, specifically suspended cantilevers or other beam topologies, have seen impressive development over the past couple decades to the achievement of attogram [1] and zeptogram [2] resolutions toward single-molecule detection [3]. This class of devices has found especially important applications in biological characterization and sensing, through the use of bio-functionalized surfaces [4]–[6] and platforms capable of single cell and single bio-particle detection [6]–[8].

A critical challenge for biological studies is maintaining physiological-support of the bio-material during measurement. Traditionally, MEMS devices either operated in a fluid medium [9] that served to suspend the sample, or samples were attached directly to the structure and dried [10] for sensing in air or vacuum. Operating in a liquid environment has a damping effect on structural oscillations, generally leading to degradation in

quality factor (Q) and the overall fidelity of resonant frequency measurements. Conversely, drying the material improves performance but prevents observation of life processes and its real-time characterization. Manalis *et al.* [5], [7] presented an elegant solution to this dichotomy by embedding a fluidic channel within a cantilever (a suspended microchannel resonator), thereby operating the MEMS device in vacuum while suspending the bio-samples within the channel's fluid volume. Suitably, the fluidic channel provides a means to serially convey bio-samples onto the MEMS structure to conduct a continuous series of measurements in consideration of sample populations or changing cell mass.

While the fluidic environment enables cell movement into and out of the device, it provokes measurement variability through an added spatial complexity. In view of the system as a harmonic oscillator, it is well-known that the resonant frequency (f_r) relates to stiffness (k) and the total effective mass (m^*) by:

$$f_r = \frac{1}{2\pi}\sqrt{\frac{k}{m^*}} \quad (1)$$

where: $m^* = m^*_{\text{structure}} + m^*_{\text{fluid}} + \alpha m^*_{\text{sample}}$

When a sample is added to the structure, position determines its contribution (α) to the effective mass of the system, dictated by the resonant modal deformation. This term gives rise to an empirically observed dependency [11], and as resonant mass sensing technologies continue to pursue meaningful results on the resolution scales previously introduced, this consideration becomes progressively more essential. The effect poses further challenges when exchanging the fluid medium of the channel, often required by pharmacology or other perturbation studies. Weng *et al.* describes using mechanical traps for this purpose [12]. However, these methods require physical interaction with the cell, typically necessitate pressure or flow change that incites instability due to pressure variations, and offer only temporary capture of the cell. Alternatively, optical trapping and manipulation has been proposed as a solution [12], [13]; however, to the authors' best knowledge, no developed platform has utilized this approach due to key challenges derived from multi-layered and complex fabrication obstacles arising from the integration of optically-clear fluidic channels for observation and manipulation (Fig. 1 illustrates a device concept).

We investigate such a platform that incorporates optical trapping techniques into this powerful class of devices, as a means to readily capture and release cells. Optical trapping also promises the potential for long-term, precise monitoring of cells or temporally-varying particles by fixing their relative position to further enhance accuracy and control over long duration measurement. Recent studies have targeted dynamic characteriza-
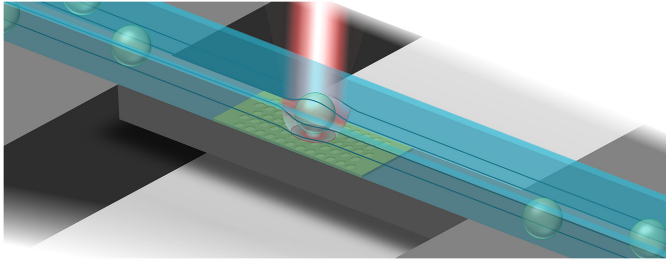
Fig. 1. Illustration of a suspended MEMS bridge resonator with a PhC, trapping/detection lasers, a trapped cell, and a fluidic channel.
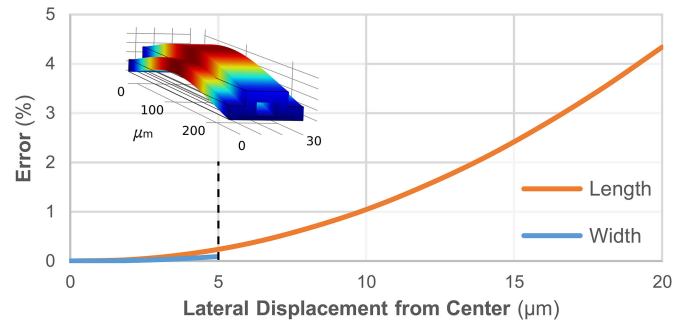

Fig. 2. Numerical simulation observing measurement error from lateral position shift along the channel length and width. The inset image shows a bridge-channel resonator model.

tion by measuring cell growth rates [14], [15] and monitoring cell response to therapeutics and interventions, but lacked a method of fine position control.

Optical tweezers do present their own set of challenges; traditional optical trapping for biological studies is limited by the susceptibility of cells to damage from the high laser intensity required. The device described in this work employs a photonic crystal (PhC) structuring of the silicon surface to enhance the trapping force, thereby necessitating less optical power and mitigating imposed biological damage, described more extensively in our previous publication [16].

II. DESIGN AND SIMULATION

Intuitively, the ratio between the sample mass and the structural mass must be maximized in the name of sensitivity, i.e., a small mass change will induce a lesser resonant frequency shift on a bulky, heavy structure. In the limit that devices become prohibitively fragile, overall device reduction is bounded when it becomes incapable of microfluidic flow or cannot accommodate samples with required inner-channel clearances. Secondly, a high Q is critical in achieving measurement stability and desired resolution. Air damping, both viscous and squeeze-film, is a significant energy dissipation mechanism at this size scale and can severely limit the quality of the resonator. In mitigation, a vacuum environment proved essential to performance, ensuring desirable frequency stability.

Material properties, including the modulus of elasticity, and optimization of the gap spacing and linear dimensions are also essential to meet design goals. Utilizing a finite element analysis (FEA) simulation (COMSOL Multiphysics) based on Navier's equations to obtain the structural eigenvalues, the chosen fixed-fixed bridge structure consisting of dimensions $1.5\,\mu m \times 33\,\mu m \times 250\,\mu m$ predicted a resonant frequency of approximately 200 kHz. The design involved a channel measuring $7\,\mu m$ (height) $\times$ $10\,\mu m$ (width), with a 5-μm thick wall. The supporting simulation shows potential to resolve mass changes with a sensitivity of about 1.1 Hz/pg at the beam center. As established in the introduction, Fig. 2 demonstrates more clearly the need for precise cell position control, showing the error (frequency shift variability) due to lateral movements in mass (1 ng in this simulation). Given the selected bridge resonator (opposing a cantilever design), lateral shifts along the channel length accumulate significant error, with higher immunity along the width (perpendicular to flow). This insight can guide opti-

cal trapping control and illuminate the role Brownian motion plays in measurement accuracy. The PhC optical trap can restrict Brownian motion below 500 nm, with potential for even greater reductions for larger cells and particles.

Optical trapping phenomenon spurs from inhomogeneity in the electromagnetic field at the focal spot, and by better confining the field, the PhC increases the trapping force, thereby requiring a lower laser intensity for a given force to yield a beneficial result for cells and other biological explorations [16]–[18]. The laser focal enhancement occurs just above the PhC with tunability offered by controlling the PhC pattern and depth. By virtue of this substrate dependency, better coupling between the vibrating resonator and trapped particle is possible.

III. FABRICATION

Device fabrication relies on a silicon-on-insulator (SOI) substrate (nominal 2-μm device and 5-μm oxide layers), where the device layer of the SOI wafer determines the thickness of the fabricated resonator. This layer enables a photolithographically defined PhC pattern, consisting of shallow holes imposed by an inductively-coupled plasma reactive-ion etch (ICP-RIE). This etch process transfers the PhC pattern into the silicon device layer with a vertical side-wall profile. Following this step is a reactive ion-etch (RIE) stopping on the buried oxide layer to define the beam structure and anchor sites, facilitating later beam release and parylene deposition, respectively.

While silicon serves as the mechanical, optical constituent, parylene-C confines fluid as the channel material, which delivers very conformal, durable coatings from chemical-vapor deposition; however, parylene typically exhibits poor adhesion to other materials, including silicon. A mitigating strategy adopted in this work to ensure reliable, robust fluidic channels, employs mechanical anchors in the silicon device layer for attachment of the parylene, which contributes to the maximum fluidic pressure and flow supported by the device, exceeding pressures of 30 psi and pump flows of 15 μL/minute. The buried oxide lends itself readily to this requirement, where etching exposes the oxide and a timed hydrofluoric (HF) etch creates sub-surface cavities. Parylene fills these voids generating points of fixation for the layer. Fig. 3 shows the cross-section of an undercut anchor cavity and its utility in maintaining attachment.
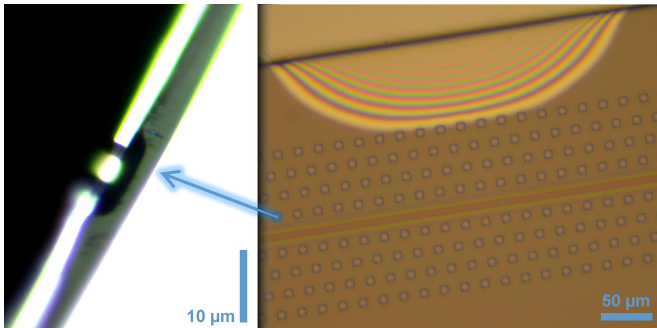
Fig. 3. The left image shows oxide-layer undercutting at each anchor site in the right image to maintain parylene adhesion.
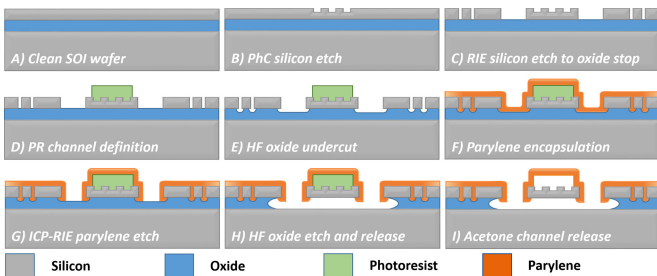

Fig. 4. A cross-section of the resonator bridge: (A) SOI wafer; (B) ICP-RIE silicon etch of the PhC into the device layer; (C) RIE silicon etch to the oxide layer defining the resonator and parylene anchors; (D) photolithography of the sacrificial photoresist channel; (E) HF oxide etch to undercut the device layer for anchor points; (F) parylene encapsulation of the photoresist/device; (G) ICP-RIE parylene etch to reveal the underlying oxide and open ports; (H) HF release of the structure; and (I) acetone dissolution of the sacrificial layer.
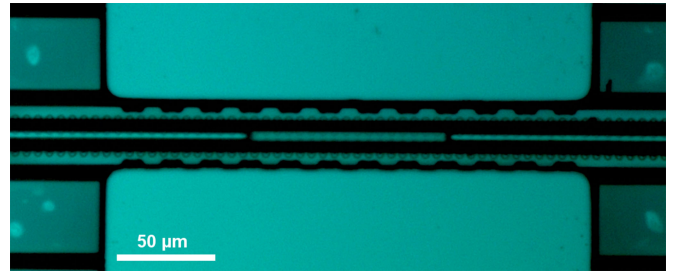

Fig. 5. MEMS bridge resonator with an integrated parylene fluidic channel (guiding fluid) and the underlying PhC.
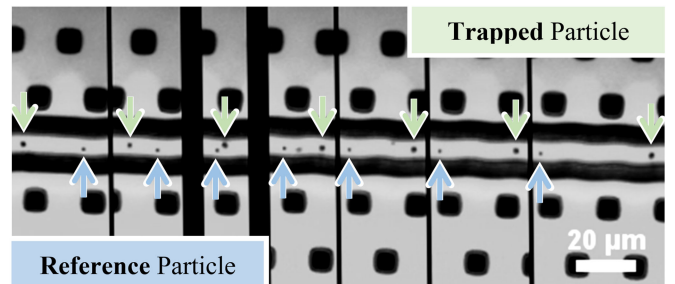

Fig. 6. Progression frames of 1-μm polystyrene beads optically trapped and manipulated within the parylene-fluidic channel (from left to right), demonstrating a critical capability of these devices.

Parylene channel formation requires a sacrificial process, and patterned thick photoresist defines the height and width of the channel, adaptable to suit various application requirements and cell types. Upon establishing this layer, chemical-vapor-deposited parylene coats the structure, encapsulating the beam resonator and the sacrificial photoresist, utilizing the cavity anchor sites for attachment. Access to the oxide layer requires an oxygen ICP-RIE etch of the parylene while simultaneously defining input and output ports for the fluidic channel. A long HF etch removes the supporting oxide sublayer to fully release the beam-channel structure, followed by a final solvent release of the channel. This process delivers a freestanding, transparent fluidic channel atop the integrated silicon PhC. Fig. 4 diagrams the fabrication process, and Fig. 5 show a final fabricated device possessing both the underlying PhC and propagating fluid within the channel volume.

IV. SETUP AND OPTICAL MANIPULATION

The structure is driven via electrostatic actuation with an electric potential applied between electrodes deposited on the front and backside of the device. The driving frequency was swept while measuring the RMS of the deflection signal to obtain the structure's frequency response. The devices operate with a DC bias of 30 V and an AC actuation voltage of 1 V_{pp}.

The optical system integrates two independent lasers to achieve simultaneous optical manipulation (Nd:YVO$_4$, Spectra-Physics, 1064 nm) and resonance detection (HeNe, Research Electro-Optics, 633 nm). To conserve space, we refer to the experimental set-up shown in [19]. Both functions occur coincidently under a microscope through introduction by a dichroic mirror. A spatial light modulator (SLM) is used to holographically shape and size the trapping beam, for additional functionality and adaptability of the implemented trapping approach. For resonance detection, a linear polarizer, a quarter-waveplate (λ/4), and a polarizing-beam splitter (PBS) maximize the intensity transmitted to a silicon photodiode after reflecting from the beam-channel device. With adequate amplification and filtering, a detection circuit retrieves the structure's vibrational signal for resonance measurement and its subsequent response to mass loading.

To demonstrate optical trapping, Fig. 6 depicts a progression of video frames sequencing the optical manipulation of a polystyrene bead suspended in fluid as it is moved along the channel length (relative to a stationary, reference particle). The ability to manipulate the particle within the channel and fix its position even in the presence of fluid pressure and flow, is a key functionality of this device.

V. MEASUREMENT AND RESULTS

The Q of the devices is quite low while operated in atmosphere (Q < 10), predominantly indicating squeeze-film and viscous air damping and their severe energy dissipative influences. To mitigate this imposition, the described experiments use a custom vacuum chamber (achieving vacuum <50 mTorr) mountable under microscope to attain at least an order of magnitude im-
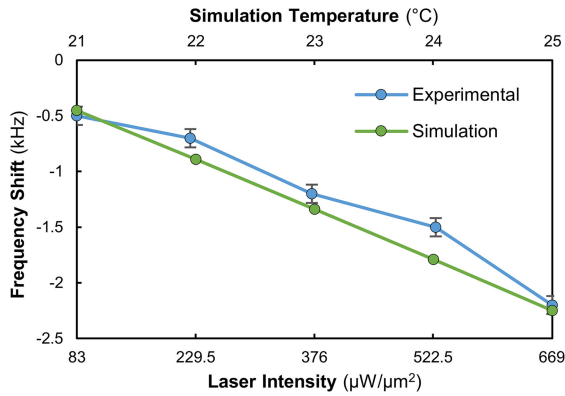
Fig. 7. Resonant frequency shift induced by the trapping laser, accompanied by a simulation of the elastic temperature dependence, necessitating control and a calibration factor during trapping measurements.
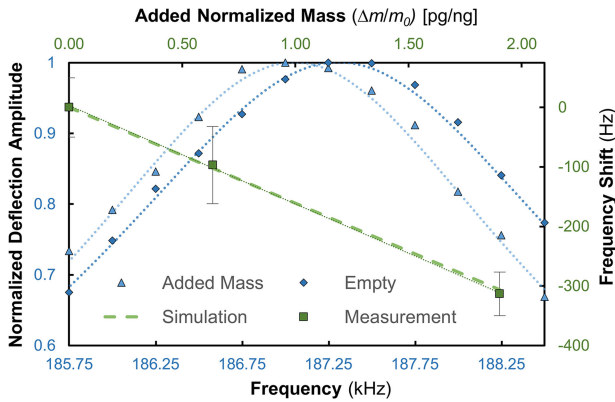

Fig. 8. Measured frequency response of an empty and a mass-loaded channel fitted by the equation for damped harmonic oscillation. The normalized deflection amplitude is the measured optical signal that exhibits proportionality to the structure's physical deflection. The measured and simulated frequency shifts incurred from added particle mass agree very closely.

provement ($Q \sim 65$), and further enhancement is important for high resolution studies.

As an experimental control, we first considered the effect of the trapping laser on the resonant frequency (Fig. 7). Since material elasticity (Young's modulus) has a temperature dependence [20], structural heating induces a proportional resonant frequency shift. For small temperature variations below the glass transition temperature, the Young's modulus has an approximately linear relationship, which dictates the trend in the structure's overall frequency response. The data in Fig. 7 provides a resonant frequency calibration for various optical trapping intensities.

To characterize the resonator's sensitivity and response to mass loading, three 5.5-μm polymer beads (each with a density of 1.05 g/cm^3) were driven to the beam-center using the manipulation laser. Particle sizes can range up to a $\sim$6 μm cross-section, with Fig. 6 showing trapped 1-μm samples. Fig. 8 observes the resonant frequency of an empty channel (fitted by the equation for damped harmonic oscillation) accompanied by a frequency shift from three-particle loading (a total mass of $\sim$274 pg); the normalized deflection amplitude is the photodiode optical signal (normalized to its peak) exhibiting proportionality to the
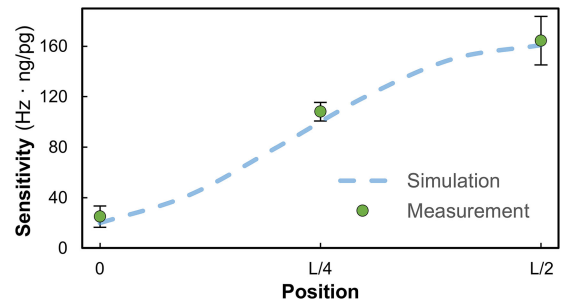

Fig. 9. Device sensitivity versus mass placement for three positions and a corresponding simulation. Both measurement and simulation validate variance due to sample position. (L is the length of the bridge structure.)

structure's physical deflection. Compared to simulated values, the plot shows good agreement: the measured sensitivity (normalized to structural mass) is 165 Hz·ng/pg, while simulation predicts 161 Hz·ng/pg. Fig. 9 verifies the sensitivity's position-dependence at its two boundaries (anchor and beam-center) and their midpoint with measurement and simulation, validating the importance of position control.

VI. CONCLUSION

The sensor described in this letter unites the techniques of optical trapping and MEMS resonant mass sensing in a microfluidic-enabled device. The achieved sensitivity of $\sim$1.14 Hz/pg, reasonably adequate for cell characterization, is comparable with the sensitivity of other published devices targeting cell applications, $0.8 \sim 1.4$ Hz/pg [15], with the added benefit of enabled optical trapping to achieve higher repeatability and accuracy, and an optically clear channel. Considerations of laser heating effects and device sensitivity, especially its positional variance, are critical in design and accurate measurement. The size scale of these devices conforms to the requirements of biological cells, including larger mammalian lines, in pursuit of important implications in fundamental biology, pharmacology, and medicine. Fundamentally, this approach is viable for devices with reduced structural mass and increased mass sensitivities, for target particles and samples on the nanoscale.

REFERENCES

[1] J. Verd, A. Uranga, G. Abadal, J. Teva, and F. Torres, "Monolithic mass sensor fabricated using a conventional technology with attogram resolution in air conditions," *Appl. Phys. Lett.*, vol. 91, Jul. 2007, Art. no. 013501.

[2] Y. T. Yang, C. Callegari, X. L. Feng, K. L. Ekinci, and M. L. Roukes, "Zeptogram-scale nanomechanical mass sensing," *Nano Lett.*, vol. 6, no. 4, pp. 583–586, Mar. 2006.

[3] A. K. Naik, M. S. Hanay, W. K. Hiebert, X. L. Feng, and M. L. Roukes, "Towards single-molecule nanomechanical mass spectrometry," *Nature Nanotech.*, vol. 4, pp. 445–450, Jun. 2009.

[4] Y. Arntz *et al.*, "Label-free protein assay based on a nanomechanical cantilever array," *Nanotech.*, vol. 14, no. 1, pp. 86–90, Dec. 2002.

[5] T. P. Burg *et al.*, "Vacuum-packaged suspended microchannel resonant mass sensor for biomolecular detection," *J. Microelectromech. Syst.*, vol. 15, no. 6, pp. 1466–1476, Dec. 2006.

[6] A. Gupta, D. Akin, and R. Bashir, "Detection of bacterial cells and antibodies using surface micromachined thin silicon cantilever resonators," *J. Vacuum Sci. Tech. B*, vol. 22, no. 6, pp. 2785–2791, Nov. 2004.

[7] T. P. Burg *et al.*, "Weighing of biomolecules, single cells and single nanoparticles in fluid," *Nature*, vol. 446, pp. 1066–1069, Apr. 2007.

[8] M. Godin, A. K. Bryan, T. P. Burg, K. Babcock, and S. R. Manalis, "Measuring the mass, density, and size of particles and cells using a suspended microchannel resonator," *Appl. Phys. Lett.*, vol. 91, no. 12, Sep. 2007, Art. no. 123121.

[9] T. Braun *et al.*, "Micromechanical mass sensors for biomolecular detection in a physiological environment," *Phys. Rev. E*, vol. 72, no. 3, Sep. 2005, Art. no. 031907.

[10] B. Ilic, Y. Yang, and H. G. Craighead, "Virus detection using nanoelectromechanical devices," *Appl. Phys. Lett.*, vol. 85, no. 13, pp. 2604–2606, Jul. 2004.

[11] S. Dohn, W. Svendsen, A. Boisen, and O. Hansen, "Mass and position determination of attached particles on cantilever based mass sensors," *Rev. Sci. Instrum.*, vol. 78, no. 10, Oct. 2007, Art. no. 103303.

[12] Y. Weng, F. F. Delgado, S. Son, T. P. Burg, S. C. Wasserman, and S. R. Manalis, "Mass sensors with mechanical traps for weighing single cells in different fluids," *Lab Chip*, vol. 11, pp. 4174–4180, Oct. 2011.

[13] R. Bashir, "Microcantilevers track single-cell mass," *Nature Biotech.*, vol. 34, no. 11, pp. 1125–1126, Nov. 2016.

[14] K. Park *et al.*, "Measurement of adherent cell mass and growth," *Proc. Nat. Acad. Sci. USA*, vol. 107, no. 48, pp. 20691–20696, Nov. 2010.

[15] N. Cermak *et al.*, "High-throughput measurement of single-cell growth rates using serial microfluidic mass sensor arrays," *Nature Biotech.*, vol. 34, no. 10, pp. 1052–1059, Oct. 2016.

[16] P. Jing, J. Wu, G. W. Liu, E. G. Keeler, S. H. Pun, and L. Y. Lin, "Photonic crystal optical tweezers with high efficiency for live biological samples and viability characterization," *Sci. Rep.*, vol. 6, Jan. 2016, Art. no. 19924.

[17] P. Jing, J. Wu, and L. Y. Lin, "Patterned optical trapping with two-dimensional photonic crystals," *ACS Photon.*, vol. 1, no. 5, pp. 398–402, Apr. 2014.

[18] B. K. Wilson *et al.*, "Nanostructure-enhanced laser tweezers for efficient trapping and alignment of particles," *Opt. Express*, vol. 18, no. 15, pp. 16005–16013, Jul. 2010.

[19] E. G. Keeler, P. Jing, J. Wu, C. Zou, and L. Y. Lin, "MEMS resonant mass sensor with enabled optical trapping," in *Proc. IEEE Int. Conf. Nano/Micro Eng. Molecular Syst.*, 2017, pp. 639–643.

[20] N. Ono, K. Kitamura, K. Nakajima, and Y. Shimanuki, "Measurement of Young's modulus of silicon single crystal at high temperature and its dependency on boron concentration using the flexural vibration method," *Jpn. J. Appl. Phys.*, vol. 39, no. 2A, pp. 368–371, Feb. 2000.